JMEPEG (2019) 28:63–78
https://doi.org/10.1007/s11665-018-3795-7

1059-9495/$19.00

Large-Scale Molecular Dynamics Simulation Studies on Deformation of Ni Nanowires: Surface Profile, Defects and Stacking Fault Width Analysis

Krishna Chaitanya Katakam, Pradeep Gupta, and Natraj Yedla

(Submitted July 3, 2018; in revised form November 17, 2018; published online December 12, 2018)

We report large-scale molecular dynamics simulation deformation studies of Ni nanowire (NW) of size 100 Å (x) × 1000 Å (y) × 100 Å (z) comprising of 925,965 atoms. Surface and internal defects are introduced to study their effect on the surface profile, strength, fracture behavior and deformation mechanisms. Tensile tests have been carried out at a temperature of 10 K and at a strain rate of 10^8 s^{-1}. Periodic boundary condition is applied along the loading direction (y). Peak strength of 23 GPa is observed in the perfect NW, and the strength decreases with defects. The surface profiles of the deformed NWs show intrusion and extrusion regions corresponding to slip steps with wider valleys in the defect NWs. Several intrinsic and extrinsic parallel stacking faults (SFs) are generated after yielding by slip occurring on {111} planes. The calculated SF widths are in the range of 0.85-2.57 nm in the perfect NW. The dislocations are mainly Shockley partial dislocations of type 1/6 ⟨112⟩, and Schmid's factor (m) obtained is 0.471. Twinning dislocation of types 1/9 ⟨221⟩ and 1/18 ⟨172⟩ is also observed in the SFs. The density of Shockley partial dislocations is observed to be the maximum in all the NWs.

Keywords dislocation density, molecular dynamics, slip system, stacking fault

1. Introduction

One-dimensional nanowires (NWs) are important building blocks in electromechanical devices, interconnects and other nanodevices (Ref 1). In such applications, the reliability of the devices depends on the mechanical response of NWs (Ref 2). NWs have a large surface to volume ratio as compared to bulk materials, so the free surfaces are expected to play an important role on the plastic deformation at smaller length scales. Molecular dynamics (MD) has become a suitable computational tool for simulating elasto-plastic deformation (Ref 1-3), failure process in crystalline (Ref 4) and non-crystalline materials (Ref 5-7), identifying deformation mechanisms (Ref 8, 9), heat transfer characteristics of nanofluids (Ref 10), deformation and melting studies of multilayers (Ref 11, 12).

Several MD simulation studies have been reported investigating the effects of size, shape, crystal orientation, temperature, strain rate and defects on the deformation behavior and deformation mechanism in Ni NWs. Paulo et al. (Ref 13) have reported that with an increase in the cross section (5 × 5 fcc unit cells-20 × 20 fcc unit cell), strength of the Ni NWs increases and the crystallinity of Ni NW is maintained only below the deformation strain rate of 0.05% ps^{-1} above which amorphization occurs. Further, they report that the results are independent of NW length beyond 35.2 Å. Wen et al. (Ref 14) studies have reported strength in the range of 8.26-8.68 GPa in Ni NWs (29.6 Å diameter × 141 Å length; temperature: 300 K) deformed in the strain rate range of 0.25 × 10^9 to 2.5 × 10^9 s^{-1}. They have also observed atomic rearrangements that cause zigzag stress–strain curve. Park et al. (Ref 8) have studied the crystal orientation and temperature effect (50–300 K) on the deformation behavior and mechanism of FCC NWs (size: 140.96 Å × 21.44 Å × 21.44 Å). They have concluded that in the crystal with ⟨100⟩ orientation, the deformation mechanism is by slip by partial dislocation motion when loaded in tension and by twinning during compression. For ⟨110⟩ orientation, the deformation mechanism is by twinning in tension. Also, they highlighted the importance of free surfaces and side surface orientations responsible for the above behavior. In the effect of strain rate study (Ref 15) at a temperature of 300 K on Ni NW of 2.53 nm diameter × 24.6 nm length (11,270 atoms), it has been reported that plastic deformation mechanism is by slip associated with Shockley partial dislocation motion and the structure remains crystalline after the yield. The reason for Shockley partial slip has been attributed to the lower energy than perfect dislocation slip. Further, they observed neck formation in the NWs before fracturing at strain rates below 5 × 10^9 s^{-1}, whereas at strain rates above 8 × 10^{10} s^{-1} the atomic structure is found to become amorphous and absence of neck formation. In the studies of Huang et al. (Ref 16), it has been reported that yield strain of Ni NWs is independent of cross sections (17.62 Å × 17.62 Å-52.86 Å × 52.86 Å) and strain rates (1.25 × 10^8 s^{-1} to 2.5 × 10^9 s^{-1}). Wang et al. (Ref 17) have reported that yield strength and elastic modulus of Ni NWs (diameter = 40-60 A and length = 150 Å) decrease with increasing temperature. Experimental tensile studies (strain rate: 10^{-4} s^{-1} to 10^{-2} s^{-1})

Krishna Chaitanya Katakam, Pradeep Gupta, and **Natraj Yedla**, Computational Materials Engineering Group, Department of Metallurgical and Materials Engineering, National Institute of Technology Rourkela, Rourkela 769008, India. Contact e-mail: yedlan@nitrkl.ac.in.

(Ref 1) on Ni NWs have revealed that smaller diameter (80-100 nm) NWs possess higher yield strength (2.5-3.5 GPa) than larger diameter wires (200-300 nm; 1.2-1.6 GPa). The reason for the above is attributed to the surface controlled dislocation process in smaller size NWs. There are few studies that report the effect of surface and internal defects on the deformation behavior and mechanism in Cu NWs (Ref 18, 19). Zhan et al. (Ref 18) report that 45° surface defect has significant effect on the strength of Cu NW and twins are observed in the defect NW. It is reported that decrease in strength of Cu NWs due to surface defects is more as compared to the internal defects; however, Young's modulus is found to be insensitive to the surface defects (Ref 19). The deformation process in the above study is by nucleation and propagation of Shockley partials and generation of twins.

All the above deformation studies report on the effect of cross section size, strain rate and temperature of perfect Ni NWs considering few thousands of atoms. Further, the studies on the defective NWs are also important as the load-bearing capacity is reduced and also the defects significantly can alter the deformation mechanisms. However, there are only a few studies that have reported on the defective (voids, vacancies) Ni NWs (Ref 4, 20). Potirniche et al. (Ref 4) have studied the void growth and coalescence in single crystal Ni comprising of 5000-170,000 atoms. The tensile tests have been carried out at strain rates in the range of 10^8 s^{-1}-10^{10} s^{-1} and at a temperature of 300 K. The results show that irrespective of void fraction, the smaller size sample exhibits higher yield strength (20.5 GPa). Also, they report that due to stress concentration at the void surface, dislocation slip is initiated and it propagates to the outer edges of the specimen. Further, they report that nucleation and evolution pattern of plastic slip is dependent on the sample size. Ferdous and Adnan (Ref 20) have reported the effect of a single surface vacancy on the strength, cross section and length of Ni NWs. In their studies, it has been observed that vacancy reduces the strength of perfect NW by 80%, whereas an increase in the cross section from 0.704 nm × 0.704 nm to 3.52 nm × 3.52 nm and varying length from 3.52 to 14.08 nm do not affect. Also, the failure strength of small length NW (3.52 nm) is lower than NW of large length (7.04 nm). A study by Makino et al. (Ref 21) has reported that a vacancy in a cylindrical Ni NW grows into a stable under equi-triaxial loading conditions.

It can be observed from the above-cited literature that there are no studies related to the effect of internal cracks, surface cracks and cracks with different orientations on the deformation behavior and mechanisms in Ni NWs. Also, a large-scale MD simulation is an extremely powerful tool in understanding the defect dynamics (Ref 22). So, in the present study, we investigate the influence of defects such as voids, internal cracks and surface cracks on the mechanical response and deformation mechanism in large-scale Ni NW using MD simulations.

2. Simulation Details

2.1 Computational Tool and Interatomic Potential

In this work, MD simulations of uniaxial tensile deformation of perfect and defect Ni NWs (NWs) have been carried out with EAM (embedded atom method) potential (Ref 23). The potential is found to fit well to basic bulk Ni properties. A comparison between the bulk properties and that predicted from potential is as follows: lattice constant (a_0) = 3.52 (Ref 24), a_0 = 3.518; elastic modulus (E) = 253 GPa (Ref 25), E = 247; bulk modulus (K) = 186 GPa (Ref 24), K = 174 GPa; cohesive energy (eV) = − 4.44 (Ref 24), − 4.389 eV. The potential is used by researchers in studying mechanical properties and structural properties (Ref 26, 27). For instance, Rezaei et al. (Ref 26) have used this potential to study the deformation twinning in Ni-graphene nanolayers. Zhang et al. (Ref 27) have studied the melting properties and nucleation of Ni under pressure. The MD simulations in the present study have been performed using the large-scale atomic/molecular massively parallel simulator (LAMMPS) (Ref 28) platform which is widely used the open-source code for studying the mechanical properties of nanocrystalline materials (Ref 29-31). MD simulations are run on High-Performance Computing (HPC) cluster (model no: HP DL360p). Simulations are run in parallel Message Passing Interface (MPI) on HPC by using 32 and 16 core, and the total wall clock time for different simulations is as follows: (a) perfect Ni NW: 381 h (32 core); (b) linear internal crack Ni NW: 225 h (16 core); (c) linear surface crack Ni NW: 293 h (16 core); (d) single void Ni NW: 203 h (16 core).

2.2 Sample Configuration Details and Tensile Deformation

Perfect Ni NW is prepared by creating a perfect FCC crystallite of Ni (cubic lattice constant a_0 = 3.518 Å) with periodic boundary conditions along the y-axis to obtain an infinitely long wire and free boundaries along the x- and z-directions (Ref 15). The NW (Fig. 1a) has initial dimensions of 100 Å (x-axis) × 100 Å (z-axis) × 1000 Å (y-axis) comprising of 925,965 atoms. After the initial construction, the sample is relaxed by the conjugate gradient method since the tensile behavior is sensitive to the initial state (Ref 15, 32). The relaxed structure is equilibrated at 10 K using Nose–Hoover thermostat (Ref 33) for 50,000 steps at a timestep of 1 fs. Similar relaxation methodology has been used in the deformation studies of FCC NWs by Park et al. (Ref 8). The relaxed structure is then deformed along y-direction [010] at a strain rate of 10^8 $s^{-1,}$ and a constant temperature of 10 K. The applied strain rate is much lower than that reported in MD simulations (Ref 32, 34) and is well suited for plasticity studies at nanoscales in metallic structures (Ref 35). Periodic boundary condition is applied along the loading direction, while the other

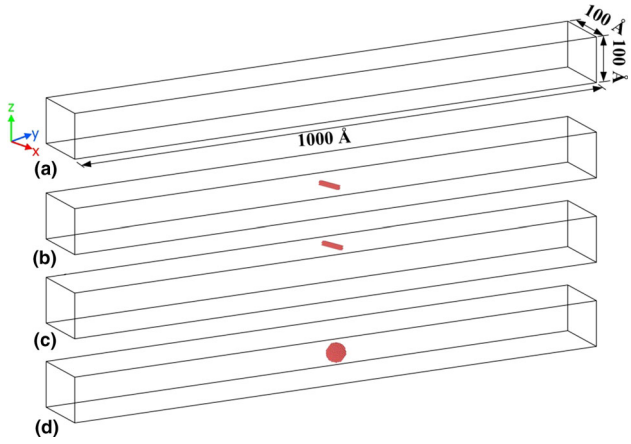

Fig. 1 Schematic of NWs of dimension 100 Å (x-axis) × 1000 A (y-axis) × 100 Å (z-axis): (a) perfect; (b) NW with linear internal crack; c) NW with linear surface crack; d) NW with void

directions are set to non-periodic. Thermodynamic ensemble NVT (where N = number of atoms, V = volume, T = temperature are kept constant) is used in the simulations. The virial stress is a measure of mechanical stress at the atomic level which has been used for calculation of tensile stress (Ref 36). The virial stress for a system of atoms is given below:

$$S^{\alpha\beta} = \frac{1}{\Omega}\left\{-\sum_i m_i v_i^{\alpha} v_i^{\beta} + \frac{1}{2}\sum_i \sum_{j \neq i} F_{ij}^{\alpha} r_{ij}^{\beta}\right\} \quad \text{(Eq 1)}$$

where Ω is the volume of the system, m_i and v_i are the mass and velocity of the atom i, F_{ij} is the force between atom i and j, r_{ij} is the distance between atoms i and j, and the indices α and β denote the Cartesian components. Strain in the sample is calculated by a change in the length of the NW upon original length (Ref 32).

2.3 Defect Analysis

Defects are identified by the coloring of atoms based on centrosymmetry parameter (CSP) introduced by Kelchner et al. (Ref 37). For the perfect crystal, the value of CSP is zero, and it increases to a positive value for defects and atoms on the surface. The above analysis is carried out using OVITO software (Ref 38), and dislocations are observed using DXA (dislocation extraction algorithm) (Ref 39). DXA is used to identify perfect dislocations, partial dislocations and secondary dislocations in fcc, bcc, semi-coherent crystal interfaces and grain boundaries. The algorithm identifies the atomic positions in the crystal and identifies that are all dislocations and determines their Burger's vector and outputs each dislocation segment as line, and its formulation method is explained in Ref. (39). Defects such as linear cracks and void are introduced by deleting atoms in the NWs as shown in Fig. 1(b), (c) and (d). Figure 1(b) shows the NW with linear internal crack (50 A length × 5 Å width × 6 Å thick). Figure 1(c) shows the NW with linear surface crack (50 Å length × 5 Å width × 6 A thick). Figure 1(d) shows the NW having a void (diameter = 30 Å) at its center. The defect NWs are subjected to a similar method of deformation as applied to perfect Ni NW.

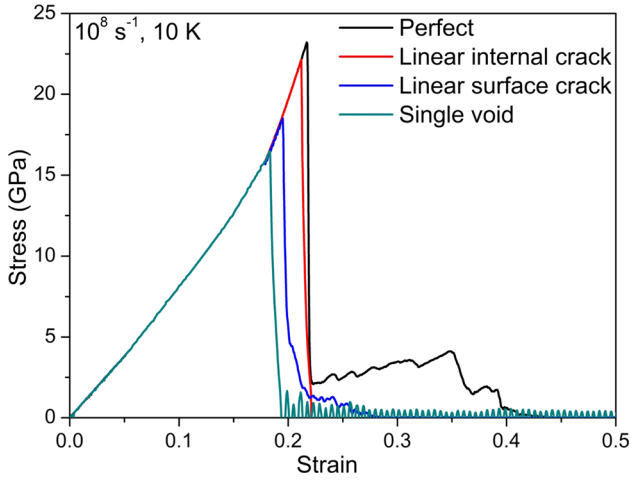

Fig. 2 Stress–strain behavior of perfect and defect Ni NWs deformed at a strain rate of 10^8 s^{-1} and at a temperature of 10 K

3. Results and Discussions

In this section, a detailed investigation is reported on the uniaxial stress–strain response, the surface profile of deformed NWs, fractographs, deformation mechanism, slip systems, stacking fault widths and evolution of dislocation density in perfect and different Ni NWs deformed at a strain rate of 10^8 s^{-1} and temperature of 10 K.

3.1 Stress–Strain Response of Perfect and Defect Ni NWs

Figure 2 shows the stress–strain response of perfect and defect Ni NWs deformed at strain rate of 10^8 s^{-1} and temperature of 10 K. The curves show a linear behavior up to maximum stress followed by a sudden drop in the stress. It is due to the onset of plastic deformation caused by dislocation slip on {111} planes along $\langle -110 \rangle$ direction. Upon straining beyond the yield strain, NWs deform plastically and fracture. However, in the case of NWs with linear internal crack and void, there is no plastic deformation which is evident from the drop in the stress to zero after the yield. Table 1 lists the elastic moduli which are calculated from the slope of the initial linear region of the stress–strain curves and that reported in the literature. Yield stress, yield strain and fracture strains of all the NWs are also shown in Table 1. We have observed Young's modulus (E) value of 126.4 GPa for the perfect NW (70 GPa in Ref 15; 90 GPa in Ref 13). The low modulus as compared to the bulk ~ 199.5 GPa (Ref 40) is due the potential used in the simulations. In the present study, for the case of perfect NW, the stress reaches a maximum of 23.21 GPa corresponding to yield strain of $e = 0.216$ which is observed to be much higher than that has been reported in other MD studies for Ni NWs. This is due to different sizes, strain rates and temperature of deformation (size = 17.62 Å × 17.62 Å × 70.48 Å, temperature = 300 K, strain rate = 6.25×10^8 s^{-1}, maximum

Table 1 Mechanical properties of perfect and defect Ni NWs

Sl. No	Nanowire	Young's modulus, GPa	Yield strength, GPa	Yield strain	Fracture strain
1	Perfect	126.4 (70) (Ref 15) (90) (Ref 13)	23.21 (21.08) (Ref 16) (11.4) (Ref 17)	0.216	0.435
2	Linear internal crack	123.1	22.15	0.214	0.218
3	Linear surface crack	107.5	18.50	0.196	0.285
4	Void	122.8	16.46	0.183	0.194

The literature values are reported in parenthesis

strength = 21.08 GPa and E = 97.95 (Ref 16); size = 49.4 Dia. × 150 Å length, temperature = 300 K; strain rate = 1.38 × 10^9 s^{-1} maximum strength = 11.4 GPa and E = 116.5 GPa (Ref 17)). The difference in the mechanical properties could also be due to the different interatomic potentials used in the MD simulations (Ref 13, 15). Furthermore, it is worth to mention that the experimental deformation studies of Ni NWs (100-300 nm diameters) have reported the strength of 1.2-3.5 GPa which is much lower and is due to lower strain rates (10^{-3} s^{-1}-10^{-4} s^{-1}) of deformation (Ref 1). With the introduction of defects such as linear internal crack, linear surface crack and void in the NW, the load-bearing capacity decreases, and therefore, a 14% maximum decrease in the elastic modulus is observed. However, there is a significant decrease in the yield stress ~ 30% lower in the NW having void than the perfect NW as the defects accelerate the yield. Also, a decrease in the yield strain and fracture strain is observed in the NWs having defects.

3.2 Deformation Relief Patterns and Fractographs

The formation of shear traces or slip lines on the surface of deformed single crystals is one of the commonly observed structural features (Ref 41, 42) and is termed as deformation relief patters. The other types of relief patterns are bands, and folds or corrugated structures (Ref 41) formed as a consequence of self-organization of shear traces during plastic deformation. To understand the deformation behavior and fracture modes of perfect and defect Ni NWs, atomic snapshots showing the deformation relief patterns are captured and discussed in the following sections. Also, the correlation between the deformation relief patterns with the surface profile on (001) surface is studied.

3.2.1 Perfect and Defect NWs. Figure 3(a) shows the atomic snapshot of the perfect Ni NW at the onset of yield (e = 0.216) characterized by dislocations originating from the edge of the NW (dashed circle and shown in enlarged image).

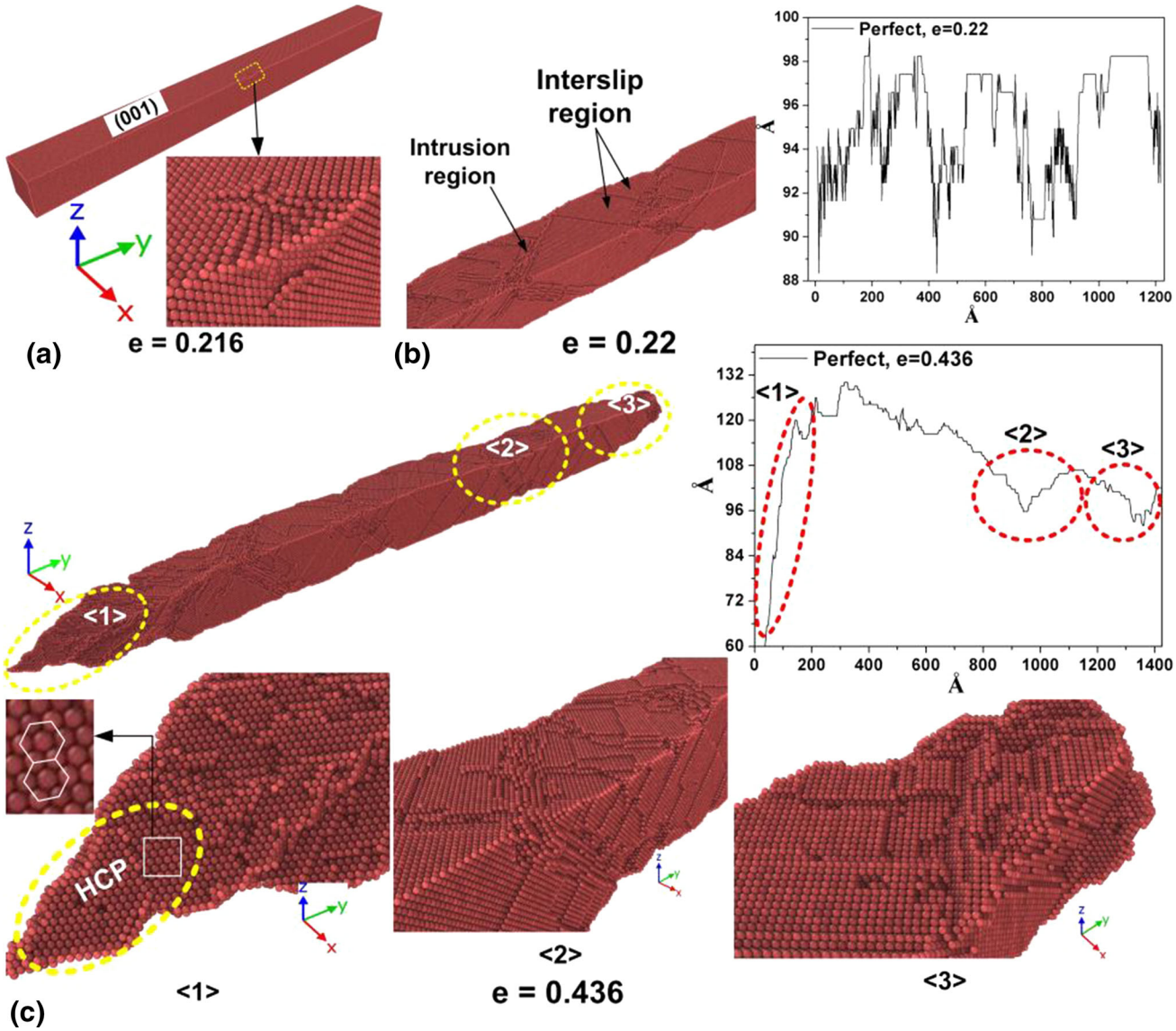

Fig. 3 Atomic snapshots of perfect NW till fracture strain and its corresponding (001) surface profile

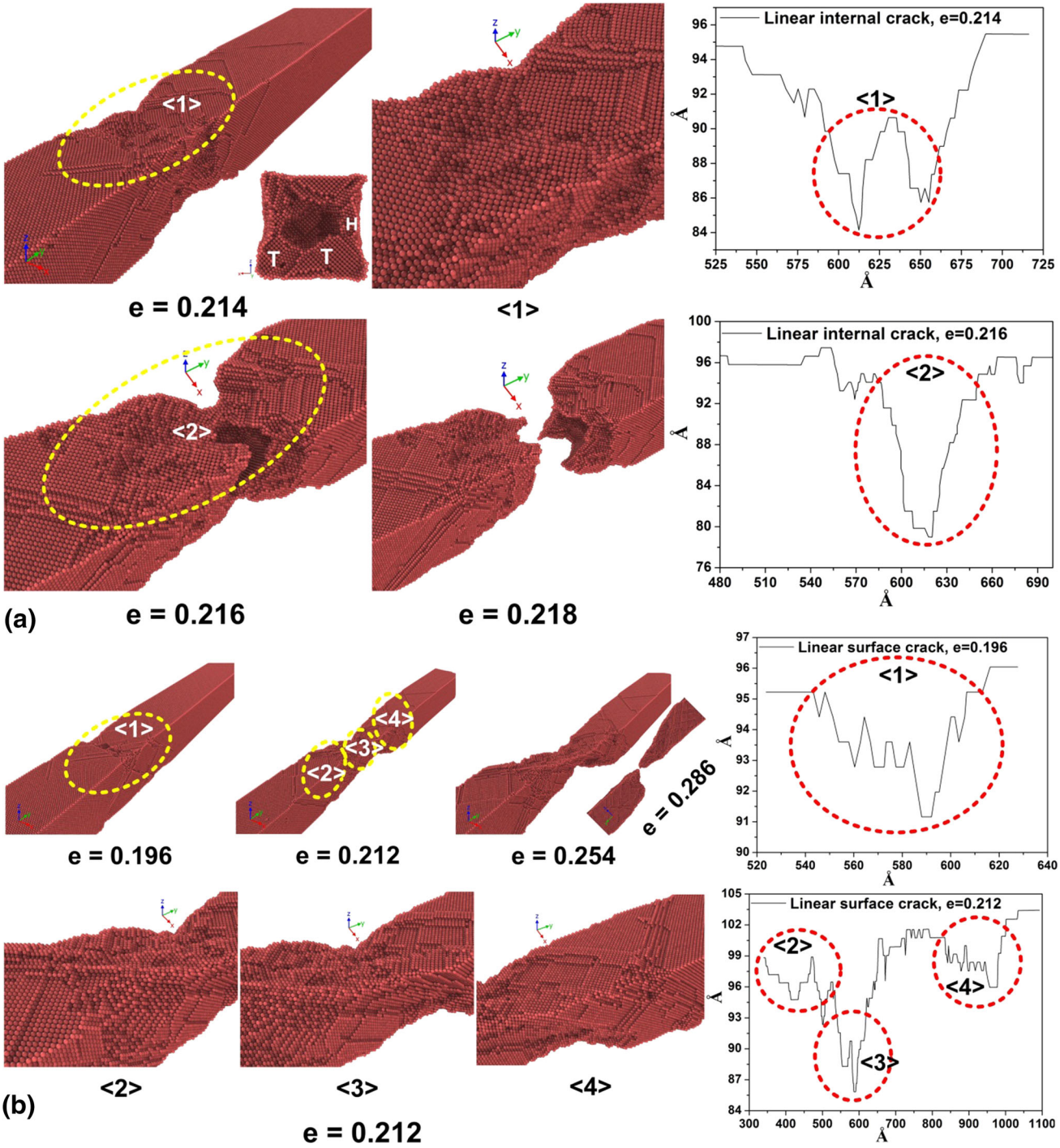

Fig. 4 Fractographs and surface profile of NWs having (a) linear internal crack (b) and linear surface crack

The subsequent plastic deformation occurs by slip occurring on multiple slip systems as seen from the slip lines on the surface at a strain of $e = 0.22$. As dislocations escape the crystal, slip steps are observed on the NW surfaces ($e = 0.22$). Also, features like inter-slip regions (marked by arrows) can be observed. The formation of shear traces on the surfaces is due to shearing on parallel octahedral planes which is the basic structural element of deformation relief (Ref 41). Experimental compressive deformation studies on Ni single crystal have also reported several types of deformation relief patterns on the surface (Ref 41, 42) The surface profile of (001) surface scanned along [010] direction of the NW at a strain of $e = 0.22$ is shown on the right. The surface reveals a quasiperiodic slip pattern formed as a result of plastic deformation by dislocation slip with well-defined extrusion areas accompanied by intrusion areas. The atomic snapshot reveals the slip steps, very wide inter-slip region and dense intrusion areas (indicated by arrow) formed by the grouping of slip steps into bundles. NW elongates and fractures at the ends by shearing at a strain of $e = 0.436$ (Fig. 3c). The fracture surface reveals a phase

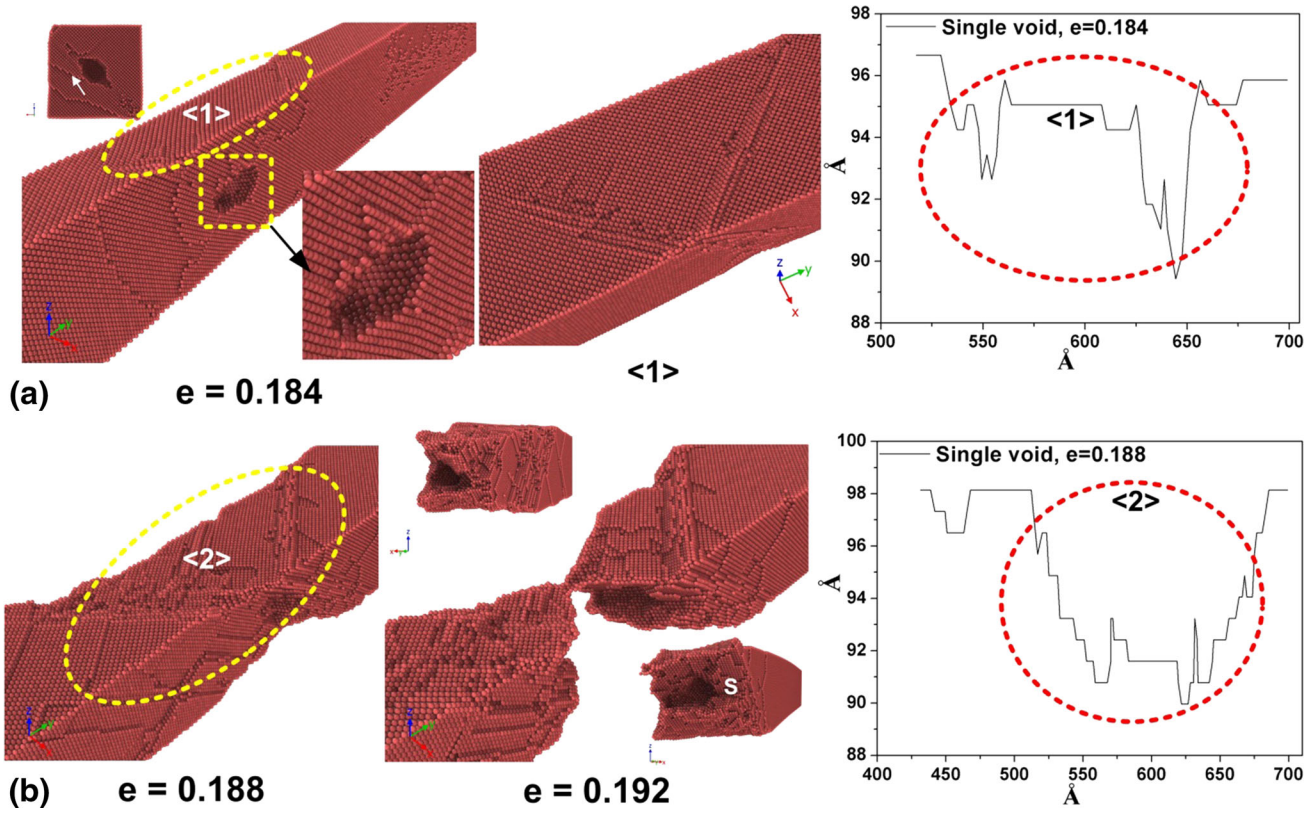

Fig. 5 Fractographs and surface profiles at different strains for the NW having a void at its center

transformation from FCC to HCP (circled region) crystal structure which could be due to the dislocation reactions which will be discussed in section "Slip Systems and Dislocation Analysis." The surface profile shown on the right for the above strain is less noisy, and intrusion regions can be seen in the enlarged atomic snapshots (⟨1⟩ ⟨2⟩ and ⟨3⟩).

In the case of defect NWs, the dislocations emerge from the defect sites due to high stress concentration (Ref 43). From the atomic snapshots captured at yield strain of $e = 0.214$ (Fig. 4a), it can be seen that the deformation is localized near the linear internal crack ⟨1⟩ and the crack expands and nearly develops to a void as seen from the cross section image. The surface comprises of several parallel and intersecting slip steps. Twinned regions (T), HCP (H) regions are observed on the face of the cross section, and also vacancies can be seen which are formed due to the annihilation of dislocations dipole (Ref 44, 45). The surface scan profile on the right shows a narrow region of intrusions and extrusions (marked by ⟨1⟩) followed by a wide valley. At a strain of $e = 0.216$, the NW necks and the surface profile (⟨2⟩) show a wide valley surrounded by a quasiperiodic structure similar to the mesoband type deformation relief observed at macroscale (Ref 42). The NW fractures at a strain of $e = 0.218$ and resembles a cup and cone type fracture as observed in ductile materials at macroscale (Ref 46). The NW with a linear surface defect (Fig. 4b) also shows similar plastic deformation features as observed in the above NW. The surface scan shown on the right for the region ⟨1⟩ at the yield strain ($e = 0.196$) shows an intense quasiperiodic structure similar to that of perfect NW. At strain of $e = 0.212$, regions marked ⟨2⟩ and ⟨3⟩ are the intrusions, while ⟨4⟩ is the extrusion and can also be visualized from the atomic snapshots. It is interesting to see that the NW gets twisted as the deformation progresses from strain $e = 0.212$ to $e = 0.254$ due to rotation of planes (⟨2⟩ till ⟨4⟩) as seen from the atomic snapshots. The NW fractures at a strain of $e = 0.286$ by shearing of atomic planes. In the NW with a void at its center (Fig. 5), at the yield strain (Fig. 5(a); $e = 0.184$) dislocations emerge from the void surface which can be clearly seen from the cross section image (indicated by arrow) and move toward the surface of the NW. The surface profile scans for region ⟨1⟩ show only few intrusion and extrusion regions, but as the strain reaches $e = 0.188$ (Fig. 5b) significant slip steps and intersecting slip steps are observed on the surface separated by wide valleys (⟨2⟩). The fracture occurs by void growth ($e = 0.192$), and the fracture surface reveals sheared planes (*S*) which are clearly visible on the cross section of the fractured NW. Similar features are also observed in the MD deformation studies on tantalum thin films (Ref 47).

3.3 Slip Systems and Dislocation Analysis

DXA analysis is carried out to identify the different types of dislocations which are represented by colored lines. For clearly identifying the types (intrinsic or extrinsic) of stacking faults (encircled regions) in the NW regions, perfect atoms are deleted from the NW and are shown separately. Figure 6 shows the CSP images, DXA analysis and different types of stacking faults observed during the deformation of perfect Ni NW at strains of $e = 0.216$, $e = 0.218$ and $e = 0.3$, respectively. It can be seen that plastic deformation occurs at the edge of the NW corresponding to yield strain of $e = 0.216$ by the emission of Shockley partial dislocations and creation of a stacking fault in between them. Such features are also reported by Huang et al. (Ref 48) in Fe and Ni NWs and for Cu NWs by Zhan et al. (Ref

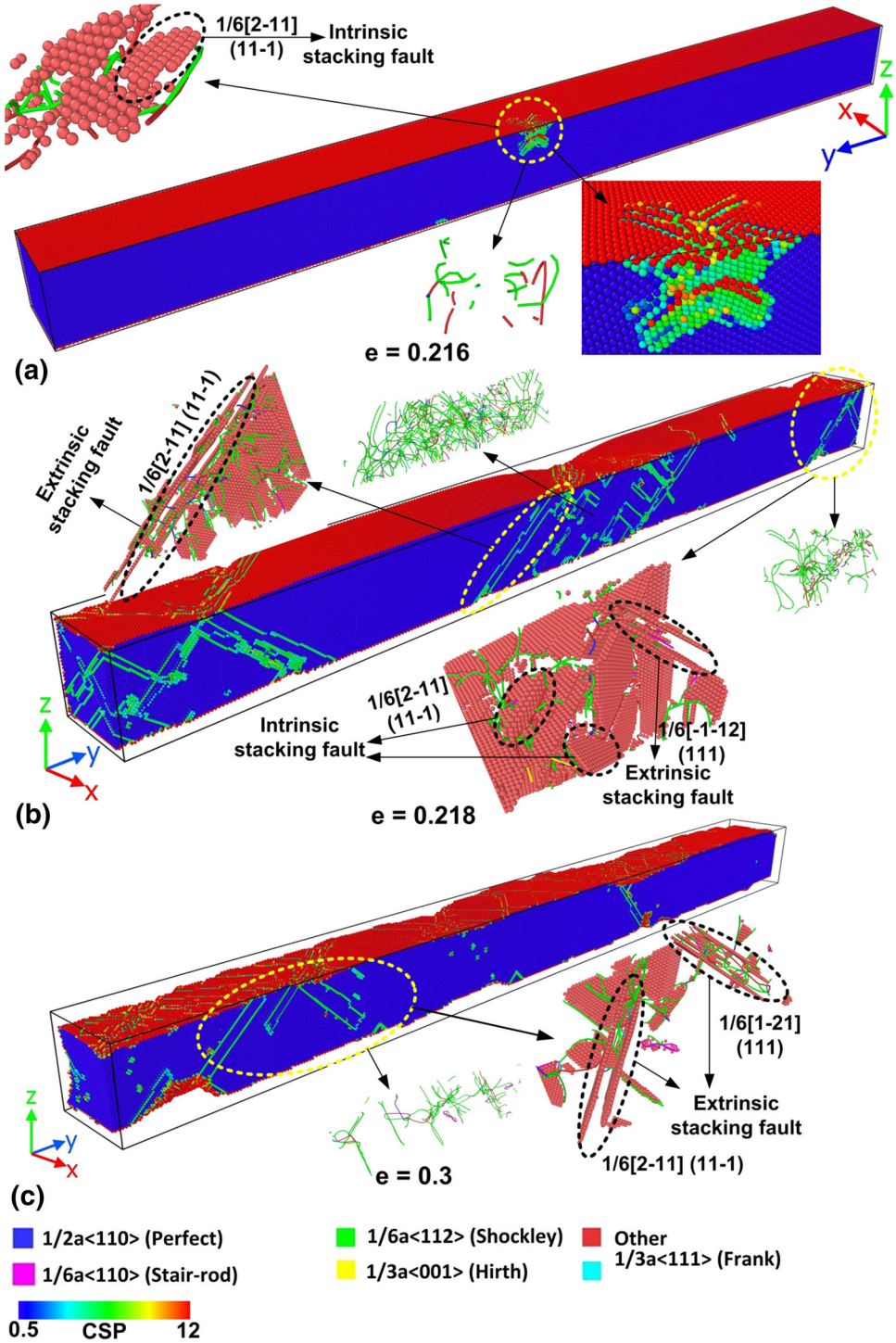

Fig. 6 CSP and DXA images and stacking faults generated in the perfect NW deformed at different strains: (a) $e = 0.216$; (b) $e = 0.218$; (c) $e = 0.3$

18). The reason for the above is because the critical shear stress for partial dislocation slip becomes lesser than perfect dislocation as the size of the specimen reaches nanoscale (10-15 nm) (Ref 49). The slip system comprising of Burger's vectors and slip plane is identified to be 1/6 [2−11] (11−1). The number of dislocations increases as the strain increases to $e = 0.218$ due to activation of slip on several slip systems, and we can see parallel stacking faults (extrinsic and intrinsic) nucleating at the edge and corners of the NW. Upon further deformation to the strain of $e = 0.3$, the defects are observed to be decreasing and could be due to the interaction between the dislocations and stacking faults causing annihilation and forming barriers (Ref 50). The DXA analysis reveals that there are six types of dislocations, namely perfect (Burger's vector: 1/2 ⟨110⟩), Shockley partial (Burger's vector: 1/6 ⟨112⟩), stair rod (Burger's vector: 1/6 ⟨110⟩), Hirth partials (Burger's vector: 1/3 ⟨100⟩), Frank partials (Burger's vector: 1/3 ⟨111⟩) and other types. Furthermore, it is observed that from the six

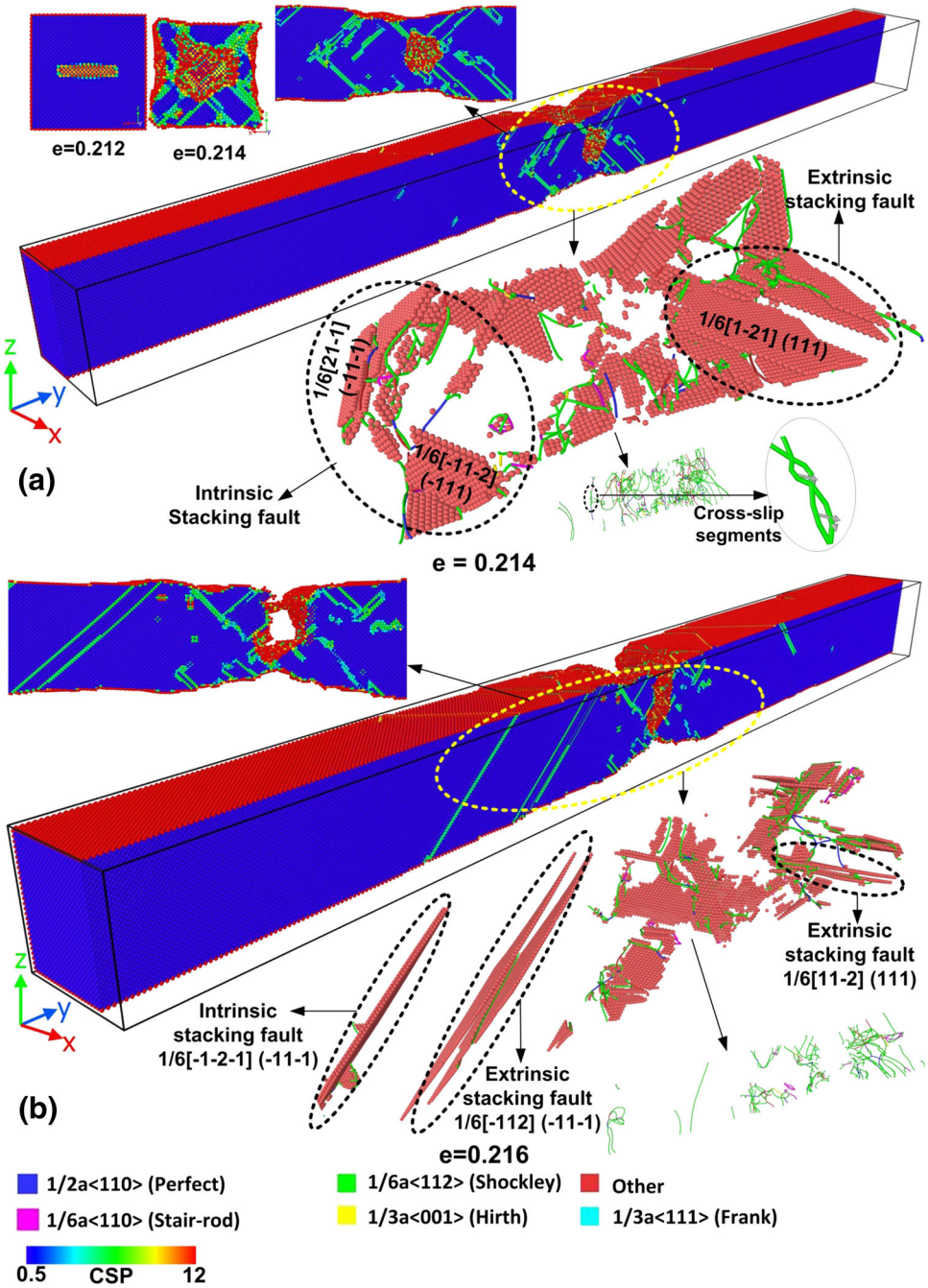

Fig. 7 CSP images, DXA analysis and stacking faults generated in the deformed NW at different strains having a linear internal crack: (a) $e = 0.214$; (b) $e = 0.216$

types of dislocations, Shockley partial dislocation is the original dislocation which is emitted from the edge of the NW and has the highest density during the whole deformation process.

Figure 7 depicts the CSP images and DXA analysis of the deformed NW having linear internal crack captured at strains of $e = 0.212$, $e = 0.214$ and $e = 0.216$. At the strain of $e = 0.212$, the crack is linear as seen from the cross section image, but as the strain reaches the yield strain ($e = 0.214$), it propagates by the emission of dislocations from its corners (Fig. 7a). Plenty of dislocations are generated which are accompanied by intrinsic and extrinsic stacking faults (encircled regions). Sung et al. (Ref 51) have shown that partial dislocation 1/6 [21−1] nucleate and slip on (−11−1) plane at the crack tip of Ni single crystal and their density increases with increase in strain. The dislocations observed are Shockley partial dislocations having Burgers vector 1/6 ⟨112⟩ type, and slippage occurs on {111} planes. Also, the stacking faults are observed to be parallel to the {111} slip planes. The true Burger's vector and Miller indices of the slip plane for few slip systems obtained in the present study are indicated in the snapshot. The DXA analysis also reveals a higher dislocation density at the yield strain than at strain of $e = 0.216$ and predominantly Shockley partial dislocations. Further, besides dislocation gliding on slip planes, we have observed cross-slip and formation of dislocation junctions ($e = 0.214$). For cross-slip to occur dislocation should be a pure screw in nature which enables to glide from one slip

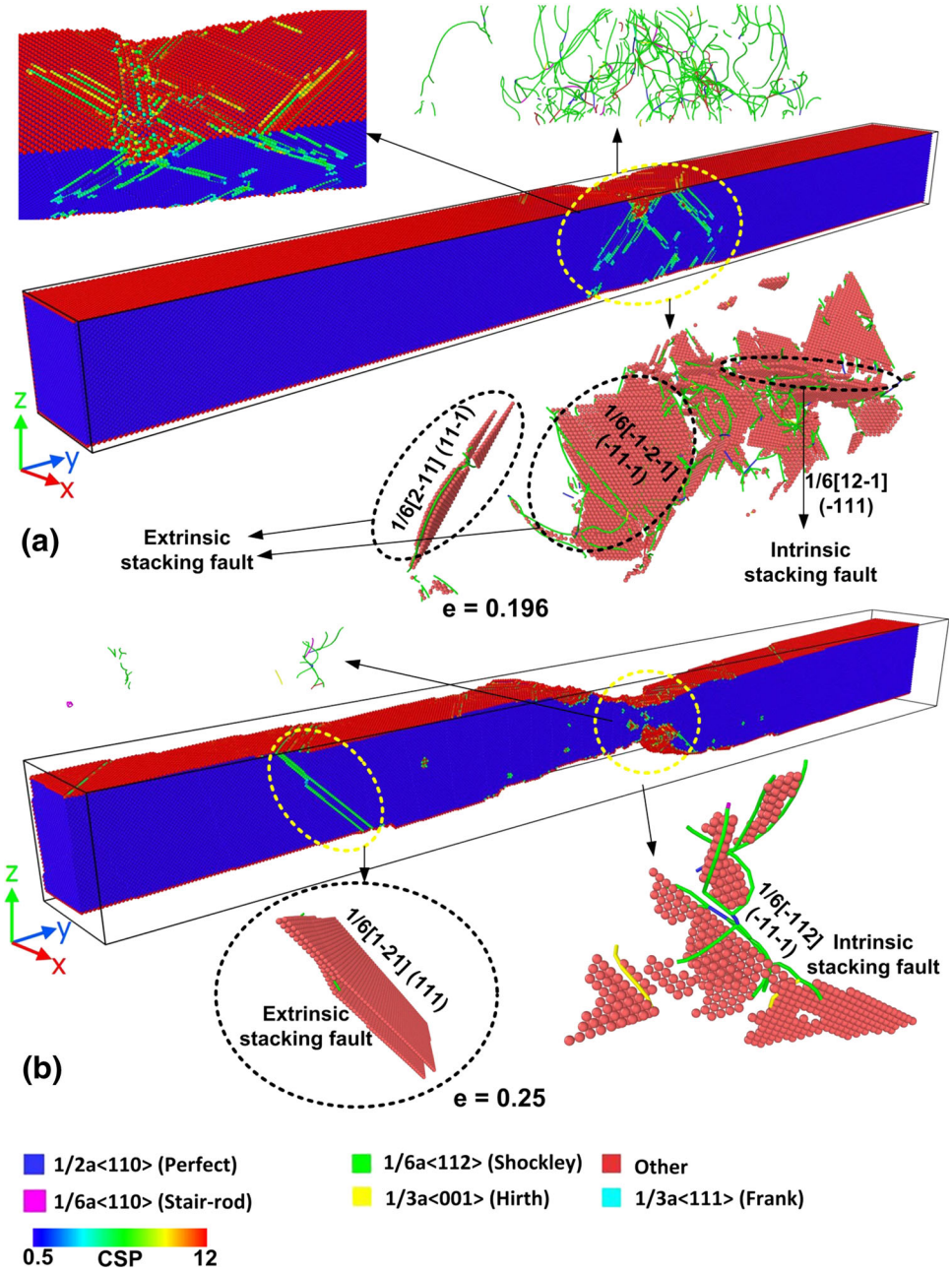

Fig. 8 CSP images, DXA analysis and stacking faults generated in the deformed NW at different strains having a linear surface crack: (a) $e = 0.196$; (b) $e = 0.25$

plane to another. Also, cross-slip is favorable in partials when their separation distance is smaller (Ref 52).

For the case of NW (Fig. 8) having linear surface crack normal to the tensile direction, dislocations emit from the corner of the crack at a strain of $e = 0.196$ and extend toward the free surface. It can also be seen that the deformation gets localized near crack as the strain increases to $e = 0.25$. Slip occurs on the {111} planes accompanied by stacking faults. The slip systems have been identified for few planes and are as follows: (−11−1) 1/6 [−112] and (111) 1/6 [1−21]. The DXA analysis shows the different types of dislocations generated at the yield strain and at a strain of $e = 0.25$. The analysis reveals six types of dislocation, and Shockley partial dislocations have the highest density.

Figure 9 shows the CSP and DXA analysis of the NW consisting of a void at its center. The dislocations appear to be originating from the void surface and able to influence the yield strain ($e = 0.184$). The void growth occurs by initiation and emission of dislocations in the same direction (Ref 4) which can be clearly seen at a strain of $e = 0.188$. Slip occurs on the {111} close-packed planes. The number of dislocations increases as the strain increases and slip extends on to few {111} adjacent planes. We have observed Lomer–Cottrell barriers which are formed due to the interaction of two gliding

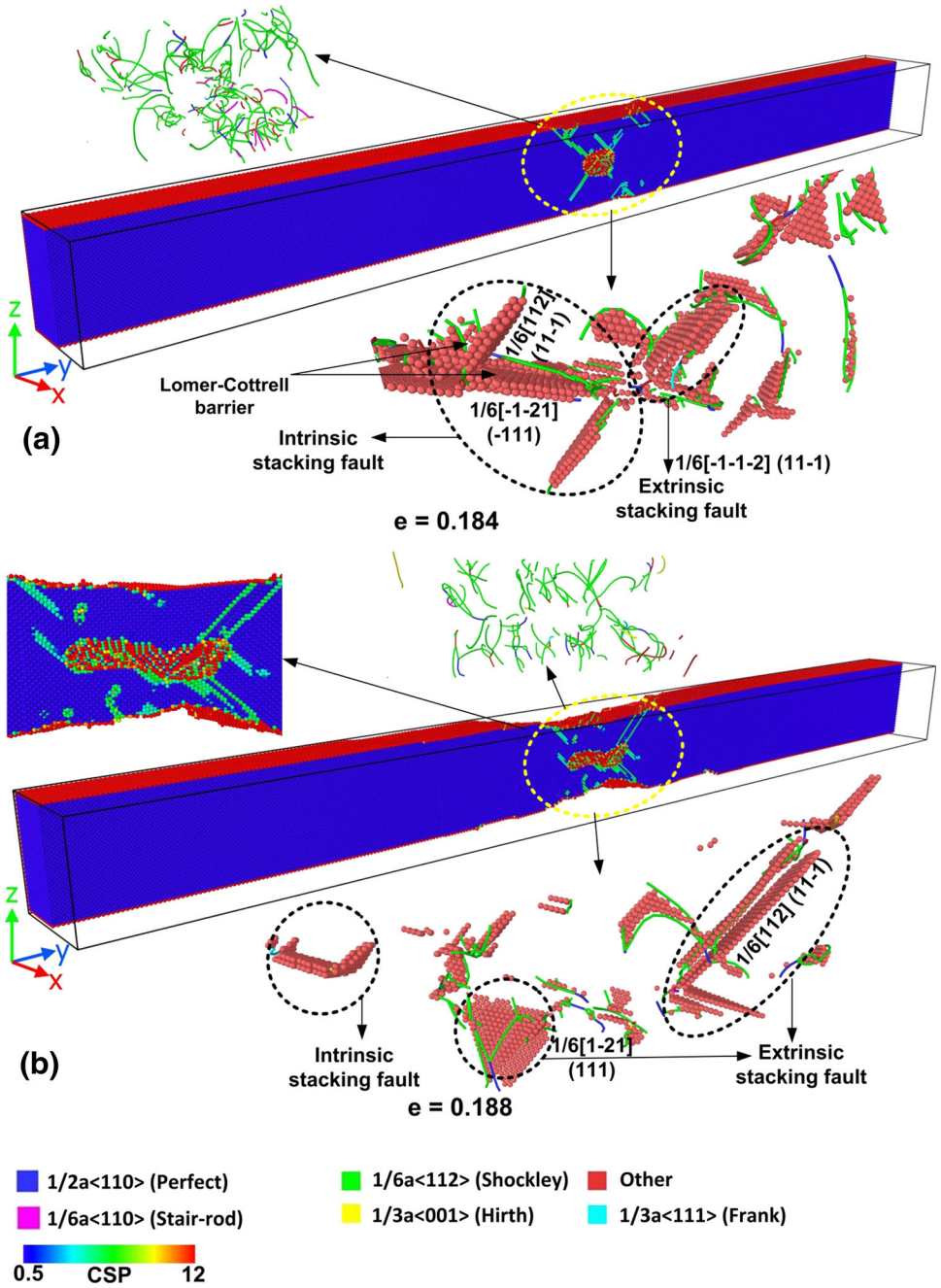

Fig. 9 CSP images, DXA analysis and stacking faults generated in the deformed NW at different strains having a void at its center: (a) $e = 0.184$; (b) $e = 0.188$

Shockley partials on two different {111} planes. The Burger's vector and Miller indices are identified to be 1/6 [112] (11−1) and 1/6[−1−21] (−111). Likewise, in the previous deformed NWs, the DXA analysis reveals several types of dislocations of which the majority is found to be Shockley partial dislocations.

3.3.1 Thompson Tetrahedron Notation. To index the Burger's vector and slip planes in the present simulation studies, Thompson tetrahedron is used as shown in Fig. 10. In Thompson tetrahedron, the points α, β, γ and δ are the centers of planes BCD, ACD, ABD and ABC, and they are used to express the four slip planes. The orientation of the Thompson tetrahedron is such that the DA direction [101] coincides with $\langle 101 \rangle$ direction (x-z plane) and the plane ABC is normal to the [111] direction. The above chosen orientation is in the accordance with that of the other simulation models (Ref 53, 54). The four slip planes, the Burger's vectors of the full slip and partial dislocations are given in Table 2.

The five types of dislocations observed in the deformed NWs are represented in the Thomson tetrahedron notation and also in the vector form. Further, we captured the DXA snapshots at strains where these reactions are observed. In the case of perfect dislocation 1/2 $\langle 110 \rangle$ for representation in

Thomson tetrahedron notation, AB is taken as an example and is shown as below.

$$AB \rightarrow A\gamma + \gamma B \quad \text{(Eq 2)}$$

Alternatively, in the vector form, the equation can be represented as follows:

$$1/2\,[-110] \rightarrow 1/6\,[-21-1] + 1/6\,[-121] \quad \text{(Eq 3)}$$

For the formation of sessile 1/6 ⟨110⟩ type dislocations, the dislocation $\beta\delta$ is taken as an example, and the following notion can be used for interaction between the Shockley partials

$$\beta C + C\delta \rightarrow \beta\delta \quad \text{(Eq 4)}$$

or in the vector form

$$1/6\,[12-1] + 1/6\,[-1-12] \rightarrow 1/6\,[011] \quad \text{(Eq 5)}$$

For the case of formation of 1/3 ⟨100⟩ type Hirth partial, the dislocation $\gamma\alpha$ is taken as an example and is represented as given below

$$\gamma B + \alpha D \rightarrow \gamma\alpha \quad \text{(Eq 6)}$$

or in the vector form, it is represented as

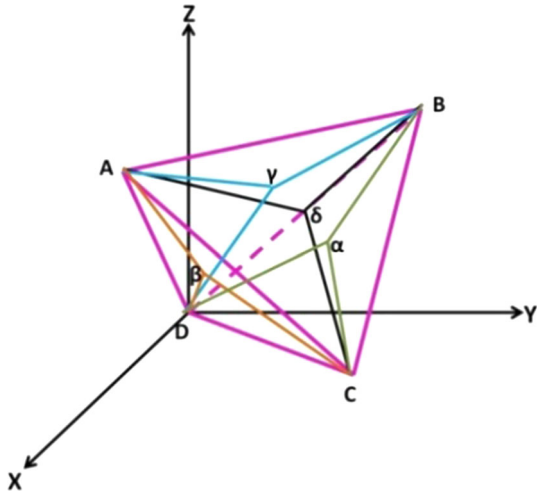

Fig. 10 Thompson tetrahedron used for the representation of slip planes and slip directions

$$1/6\,[-121] + 1/6\,[-1-2-1] \rightarrow 1/3\,[-100] \quad \text{(Eq 7)}$$

In the case of formation of 1/3 ⟨111⟩ Frank partials, the Aα dislocation is taken as an example and is represented as follows:

$$AB + B\alpha \rightarrow A\alpha \quad \text{(Eq 8)}$$

In the vector form, the above equation is represented below

$$1/2\,[-110] + 1/6\,[1-1-2] \rightarrow 1/3\,[-11-1] \quad \text{(Eq 9)}$$

All the above reactions observed follow the energy condition, i.e., the energy before the reaction is more than that after the reaction. Apart from the above five dislocations, there are other types of dislocations that are uncommon and formed as result of interactions among the five different types of dislocations. These dislocations include 1/3 ⟨211⟩ and twinning dislocations such as 1/9 ⟨221⟩, 1/9 ⟨115⟩, 1/18 ⟨255⟩, 1/18 ⟨114⟩ and 1/18 ⟨172⟩ formed due to stacking faults.

1/3 ⟨211⟩ type dislocations are the result of reactions between 1/2 ⟨110⟩ perfect and 1/6 ⟨112⟩ Shockley partials. The AB/Cδ dislocation is used to represent the above dislocation as given below

$$AB + C\delta \rightarrow AB/C\delta \quad \text{(Eq 10)}$$

In the vector form, it is as follows:

$$1/2\,[-110] + 1/6\,[-1-12] \rightarrow 1/3\,[-211] \quad \text{(Eq 11)}$$

Figure 11(a), (b), (c), (d) and (e) show the DXA snapshots of NWs at which the above-mentioned five types of dislocations are observed at a particular strain. Figure 11(a) shows the dissociation of perfect dislocation 1/2[−1−10] into two Shockley partials of type 1/6 ⟨112⟩ observed in linear surface crack NW at a strain of $e = 0.196$. Figure 11(b) shows the DXA snapshot of perfect NW at the strain of $e = 0.218$ which shows the formation of sessile stair rod dislocation 1/6 [101] from the reaction between two Shockley partials. Figure 11(c) shows the DXA snapshot of formation of sessile Hirth partial of type 1/3 [0−10] from the interaction between two Shockley partials at the strain of $e = 0.214$ in the case of NW having a linear internal crack. Figure 11(d) shows the DXA snapshot of formation of sessile Frank partial of type 1/3 [−1−1−1] from the interaction between perfect dislocation and Shockley partial at the strain of $e = 0.214$ in the case of NW having a linear

Table 2 Slip planes and directions represented on Thompson tetrahedron

Slip plane	Vector	Full dislocation	Vector	Partial dislocation	Vector
ABC	Dδ	AB	1/2[−110]	δC	1/6[11−2]
(d)	(111)	BC	1/2[10−1]	δA	1/6[1−21]
		CA	1/2[0−11]	δB	1/6[−211]
ABD	Cγ	AB	1/2[−110]	γD	1/6[−1−1−2]
(c)	(11−1)	DA	1/2[101]	γB	1/6[−121]
		DB	1/2[011]	γA	1/6[2−11]
BCD	Aα	DC	1/2[110]	αB	1/6[−112]
(a)	(1−11)	BC	1/2[10−1]	αD	1/6[−1−2−1]
		DB	1/2[011]	αC	1/6[21−1]
ADC	Bβ	DC	1/2[110]	βA	1/6[1−12]
(b)	(−111)	DA	1/2[101]	βC	1/6[12−1]
		AC	1/2[01−1]	βD	1/6[−2−1−1]

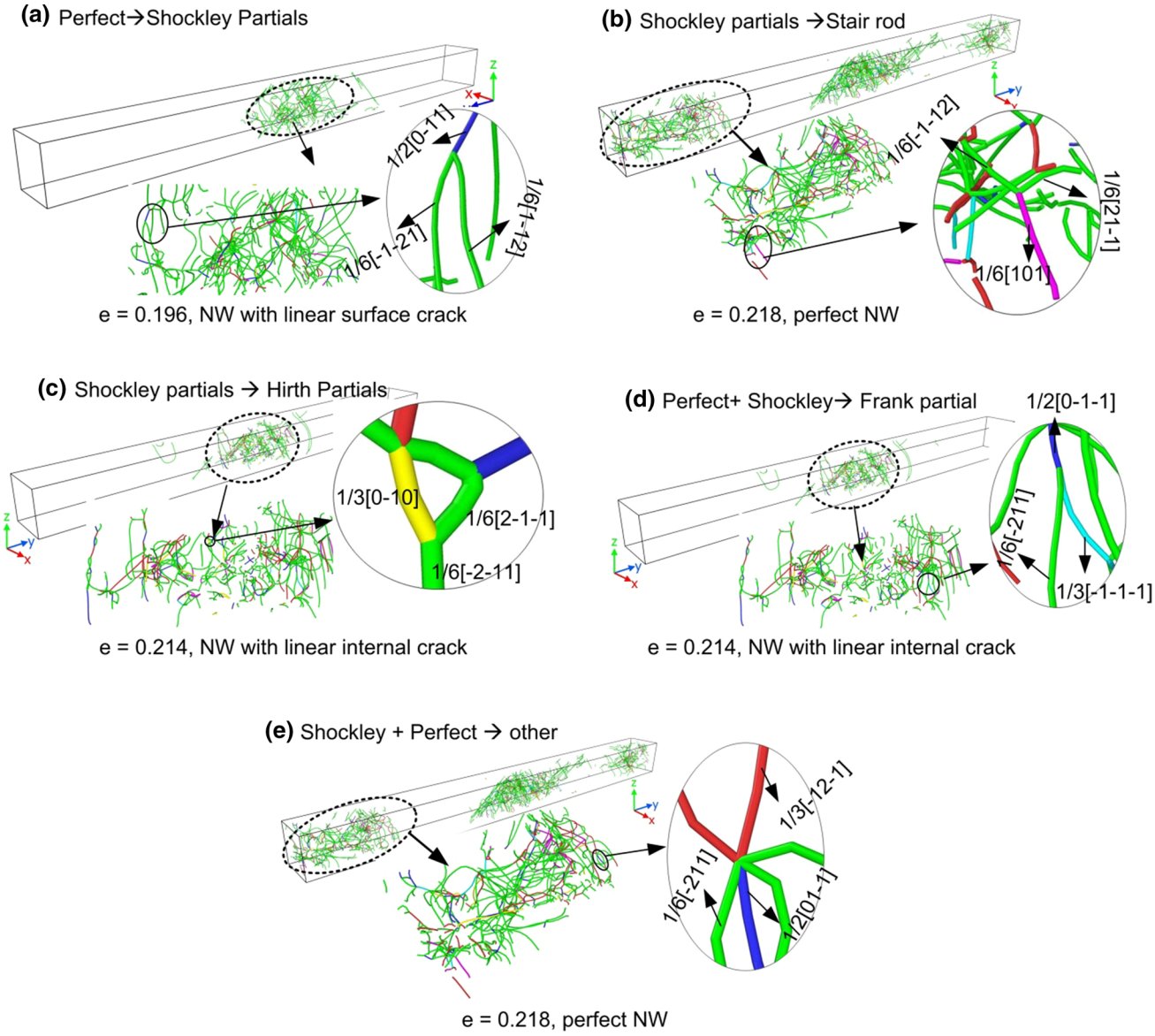

Fig. 11 (a)-(e) DXA snapshots of NWs at which five types of dislocations are observed at a particular strain

internal crack. Figure 11(e) shows the DXA snapshot of formation of sessile 1/3 [−12−1] at the strain of $e = 0.218$ in the case of perfect NW.

Figure 12 shows the mechanism of formation of twinning dislocations caused by stacking faults. Twinning dislocations are a result of the interaction of dislocations on {111} planes with the twin boundaries and are located in the regions between these twin boundaries. As a consequence, these are symmetrical products of dislocations on {111} planes. We observed twin dislocations having Burgers vector 1/18 [1−72] and 1/9 [−212] in perfect NW at strain $e = 0.3$ (Fig. 13). Formation of twin dislocations is also reported in Refs. (Ref 55-57). In the present study, as an example, we chose the twin dislocation 1/18 [1−72] which is the symmetrical vector of the dislocation 1/6 [−121] (11−1) about slip plane (111).

It can be observed from the above dislocation analysis that most of the dislocations in all the deformed NWs are partial dislocations. It is because slip in FCC crystals occurs on {111} close-packed planes, where the dislocation slip requires higher energy and leads to greater distortion of the lattice than the slip by partial dislocations (Ref 57). Hence, partial dislocations are easily nucleated in FCC crystals. It is well known that partials contain stacking faults as they are the boundaries of the stacking faults (Ref 57-59) and we have observed several stacking faults as shown in Fig. 6, 7, 8 and 9. Based on the slip systems identified, and for [010] loading direction, Schmid's factor (m) for the partial dislocation slip system (11−1)1/6[−121] obtained is 0.4714. A lower value of $m = 0.235$ is also observed in few slip systems (−111)1/6[−11−2]. For the twin system of type 1/18 ⟨552⟩, we have observed a value of $m = 0.3928$. The results are in agreement with that reported in the studies on nanotwinned copper in Ref 60. It is well known that for perfect dislocation slip system 1/2 ⟨110⟩ {111} along [010] loading direction will produce eight active slip systems having $m = 0.408$ and the rest four will have $m = 0$ (Ref 52). So, in the present study it can be inferred that partial dislocation slip is predominant.

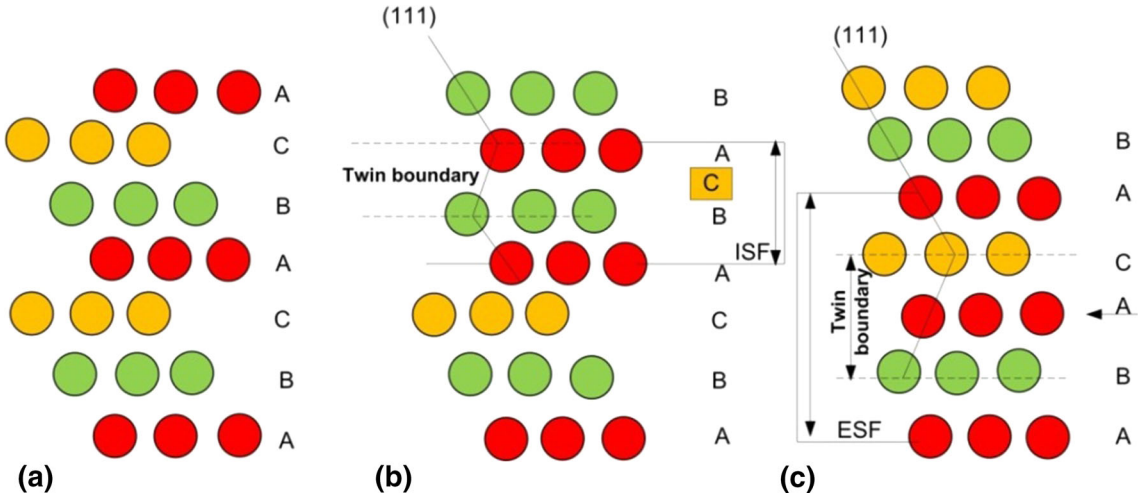

Fig. 12 Schematic showing the mechanism of formation of twinning dislocations induced by stacking faults: (a) perfect crystal; (b) crystal with intrinsic stacking faults (ISF); (c) Crystal with extrinsic stacking faults (ESF)

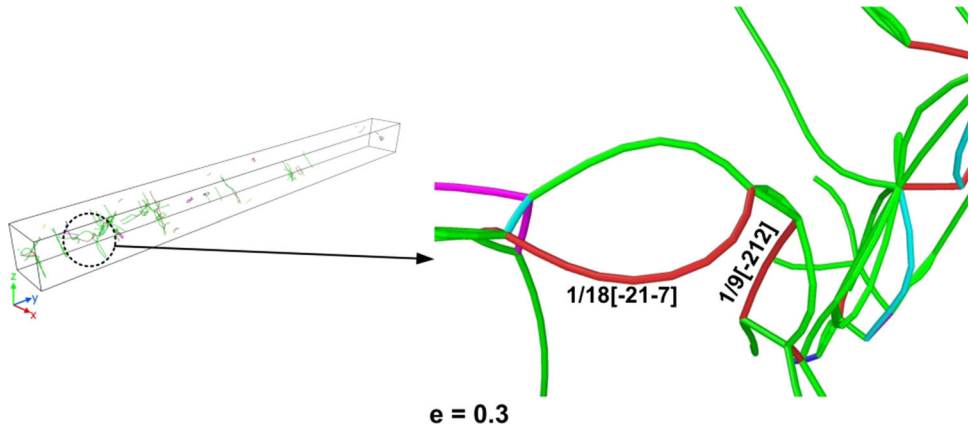

Fig. 13 Burges vectors of twinning dislocations that are observed in perfect NW at a strain of $e = 0.3$

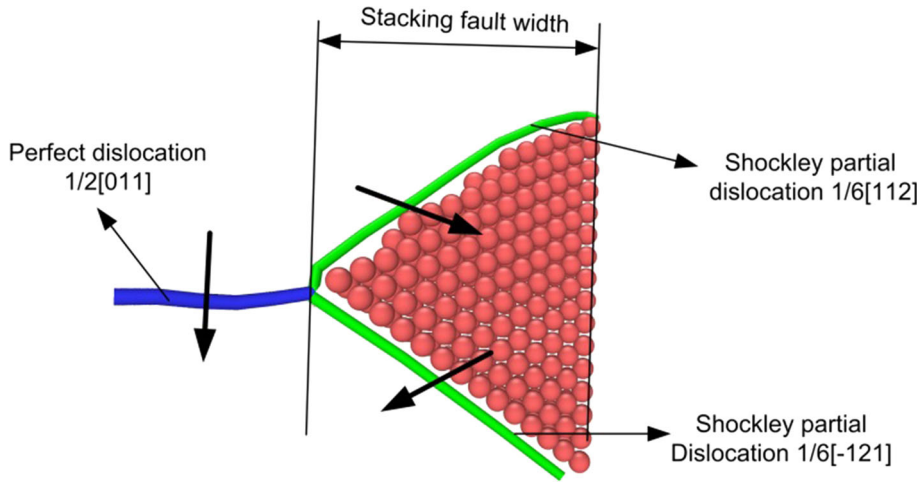

Fig. 14 Schematic showing the dissociation of perfect dislocation 1/2 [011] into two 1/6 [−121] and 1/6 [112] 60° Shockley partials on (11−1) slip plane containing the stacking fault and also representing the stacking fault width

Table 3 Stacking fault widths in the perfect and defect Ni NWs at the yield strains

Nanowire	Strain	Stacking fault width range, nm
Perfect	0.216	0.86–2.57, (2 nm) (Ref 62)
Linear surface crack	0.196	1.074–4.72
Linear internal crack	0.214	1.074–6.01
Single void	0.184	1.504–6.01

The literature value is reported in the parenthesis

3.4 Stacking Fault Widths

As observed from the above sections, SFs play a vital role on the mechanical behavior and microstructure. It is reported that the SF width effects the dislocation processes and hence the mechanical properties (Ref 58, 61). Further, SF width is not a fixed quantity for a given material and is affected by the internal stresses and arrangement of dislocations. So, in the present study we have estimated the SF widths as calculated in experiments, i.e., multiplying the number of atoms that deviate from the perfect lattice position by the distance between the two atoms (Ref 58) for the perfect and defect NWs at the respective yield strengths. Figure 14 shows the snapshot of dissociation of perfect dislocation 1/2 [011] into two 60° Shockley partials on (11−1) slip plane containing the stacking fault and also representing the stacking fault width.

We found 0.86-2.57 nm wide SFs in the perfect NW and the range of the SF width increase with the presence of defects in the NW. Wider SFs are observed in the NWs with void as a defect as compared to the other defective NWs which could be due to the difference in the internal stresses (Ref 58), their interaction with dislocations (Ref 61). This is also evident from the stress–strain curve. The range of SF widths obtained in perfect and defect NWs are tabulated in Table 3. Hunter and Beyerlein (Ref 62) have reported an equilibrium stacking fault width of 2 nm in Ni based on the MD-DFT (density functional theory) studies. Further, the SFE (stacking fault energy) reported experimentally in conjunction with the anisotropic elasticity theory is in the range of 120-130 mJ/m^2 (Ref 63). However, there are studies that have reported SFE as low as 79 mJ/m^2 and highest value of 450 mJ/m^2 (Ref 63). In the present study, we have estimated the SFE using the equation $\gamma = \frac{Ga_0^2}{48\pi r_e}\left(\frac{2+\upsilon}{1-\upsilon}\right)$ (Ref 45, 64) (where γ is the SFE; G = shear modulus; a_0 = lattice constant; r_e = equilibrium separation between the partials and υ = Poisson ratio) considering the dissociation of pure edge dislocation into Shockley partials and the above calculated SF widths. The SFE is found to be in the range of 69-207 mJ/m^2 for perfect NW which is in good agreement with the literature. Also, the SFE predicted from the interatomic potential is in the range of experiments and other interatomic potentials (Ref 65).

3.5 Dislocation Density

Figure 15 shows the influence of defects on the evolution of density of the six types of dislocations at the corresponding yield strains. It can be seen that defects have a significant effect on the evolution of different types of dislocations. In all the NWs, the density of Shockley partial dislocations which are glissile in nature possesses the largest proportion (2.49 × 10^{16}/m^2-6.72 × 10^{16}/m^2) and enhances the deformation by slip

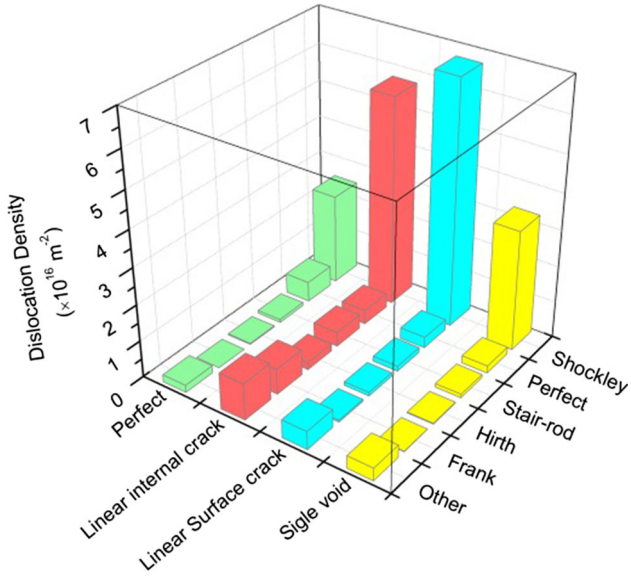

Fig. 15 Dislocation densities of six types of dislocations in the NWs at the yield strains

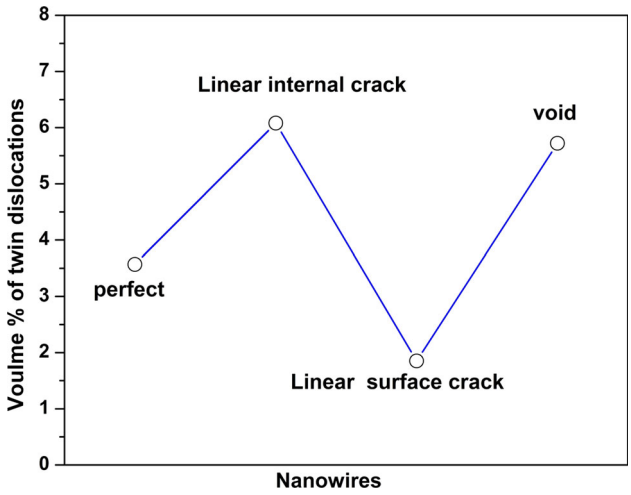

Fig. 16 Twin dislocation volume fraction at the yield strains in different NWs

ability of Ni NWs. It is also evident in the NW with linear surface crack having the large fracture strain as compared to the other defective NWs. Shockley partial dislocation density of 5 × 10^{16}/m^2 is observed in the Ni single crystal having single void (Ref 57) which is higher as compared to that obtained in the present study (3.3 × 10^{16}/m^2). It is well established that dislocation density increases with increase in strain rate (Ref 66, 67). So, in the present study a low dislocation density is observed as compared with the studies of Zhang et al. (Ref 57). Further, the model sizes and the boundary conditions are also different. We have estimated the volume fraction of twin dislocations which are categorized as one of the other dislocations. Figure 16 shows the volume fraction of twinning dislocations at the yield strains in all the NWs. As estimated, the volume fraction is found to be highest in the NW with linear internal crack and is also evident from the DXA, dislocation density analysis.

4. Conclusions

MD simulations deformation studies have been carried out on NWs consisting of different types of surface and internal defects mainly to investigate their effect on the mechanical properties, surface profile, fracture and dominant deformation mechanisms using characterization methods like CSP and DXA, and finally the evolution of dislocation density. Based on the above we conclude that the defects lower the yield stress and it is more significant ($\sim$ 30% decrease) in the NW having an internal void. However, there is not much effect on Young's modulus. The surface scans of different NWs show intrusion and extrusion regions as observed in bulk. In the case of NW with defects, wide valleys are observed due to localized deformation in the defect regions of the NW. The fractographs show shear type of fracture in the perfect and linear surface crack NWs, whereas, in the case of NWs with void and linear internal crack, the deformation is localized and resembles a cup and cone type fracture. However, the plastic strains are very less indicating their brittle nature. Several intrinsic and extrinsic parallel stacking faults are observed during deformation in all the NWs accompanied by six types of dislocations of which the Shockley partial dislocation has the highest density. We have also observed cross-slip mechanism and twinning. It is also observed that the stacking fault widths increase in the presence of defects. From the Schmid's factor calculations, a maximum value of $m = 0.471$ and $m = 0.392$ is obtained for the partial dislocation slip system and twin slip system, respectively. So, it can be concluded that the dominant deformation mechanism is by slip by partial dislocation glide.

Acknowledgments

The authors would like to acknowledge Department of Science and Technology, India, for their support (DST No: YSS/2014/000985).

References

1. C. Peng, Y. Zhong, Y. Lu, S. Narayanan, T. Zhu, and J. Lou, Strain Rate Dependent Mechanical Properties in Single Crystal Nickel Nanowires, *Appl. Phys. Letts*, 2013, **102**, p 83102
2. T. Zhu, J. Li, A. Samanta, A. Leach, and K. Gall, Temperature and Strain-Rate Dependence of Surface Dislocation Nucleation, *Phys. Rev. Lett.*, 2008, **100**(2), p 1–4
3. P. Gupta, S. Pal, and N. Yedla, Molecular Dynamics Based Cohesive Zone Modeling of Al (metal)-Cu 50 Zr 50 (Metallic Glass) Interfacial Mechanical Behavior and Investigation of Dissipative Mechanisms, *Mater. Des.*, 2016, **105**, p 41–50
4. G.P. Potirniche, M.F. Horstemeyer, G.J. Wagner, and P.M. Gullett, A Molecular Dynamics Study of Void Growth and Coalescence in Single Crystal Nickel, *Int. J. Plast*, 2006, **22**(2), p 257–278
5. D.K. Das and M.M. Ghosh, On Mechanical Properties of Graphene Sheet Estimated Using Molecular Dynamics Simulations, *J. Mater. Eng. Perform.*, 2017, **26**(9), p 4522–4532
6. N. Yedla, P. Gupta, T.Y. Ng, and K.R. Geethalakshmi, Effect of Loading Direction and Defects on the Strength and Fracture Behavior of Biphenylene Based Graphene Monolayer, *Mater. Chem. Phys.*, 2017, **202**, p 127–135
7. M. Grujicic, R. Yavari, J.S. Snipes, S. Ramaswami, T. Jiao, and R.J. Clifton, Experimental and Computational Study of the Shearing Resistance of Polyurea at High Pressures and High Strain Rates, *J. Mater. Eng. Perform.*, 2015, **24**(2), p 778–798
8. H.S. Park, K. Gall, and J.A. Zimmerman, Deformation of FCC Nanowires by Twinning and Slip, *J. Mech. Phys. Solids*, 2006, **54**(9), p 1862–1881. https://doi.org/10.1016/j.jmps.2006.03.006
9. A. Movahedi-Rad and R. Alizadeh, Dependence of Strain Rate Sensitivity on the Slip System: A Molecular Dynamics Simulation, *J. Mater. Eng. Perform.*, 2017, **26**(11), p 5173–5179
10. M.M. Ghosh, S. Ghosh, and S.K. Pabi, Effects of Particle Shape and Fluid Temperature on Heat-Transfer Characteristics of Nanofluids, *J. Mater. Eng. Perform.*, 2013, **22**(6), p 1525–1529
11. H.Y. Song, J.J. Xu, Y.G. Zhang, S. Li, D.H. Wang, and Y.L. Li, Molecular Dynamics Study of Deformation Behavior of Crystalline Cu/amorphous Cu50Zr50 Nanolaminates, *Mater. Des.*, 2017, **127**, p 173–182
12. F. Baras, V. Turlo, and O. Politano, Dissolution at Interfaces in Layered Solid-Liquid Thin Films: A Key Step in Joining Process, *J. Mater. Eng. Perform.*, 2016, **25**(8), p 3270–3274
13. P.S. Branı, Large Deformation and Amorphization of Ni Nanowires under Uniaxial Strain—A MD Study - Branicio_Rino _ Phys Rev B 62 (2000) 16950, 2000, **62**(24), p 950–955
14. Y.H. Wen, Z.Z. Zhu, G.F. Shao, and R.Z. Zhu, The Uniaxial Tensile Deformation of Ni Nanowire: Atomic-Scale Computer Simulations, *Phys. E Low-Dimens. Syst. Nanostruct.*, 2005, **27**(1–2), p 113–120
15. Y.H. Wen, Z.Z. Zhu, and R.Z. Zhu, Molecular Dynamics Study of the Mechanical Behavior of Nickel Nanowire: Strain Rate Effects, *Comput. Mater. Sci.*, 2008, **41**(4), p 553–560
16. D. Huang, Q. Zhang, and P. Qiao, Molecular Dynamics Evaluation of Strain Rate and Size Effects on Mechanical Properties of FCC Nickel Nanowires, *Comput. Mater. Sci.*, 2011, **50**(3), p 903–910
17. W.D. Wang, C.L. Yi, and K.Q. Fan, Molecular Dynamics Study on Temperature and Strain Rate Dependences of Mechanical Tensile Properties of Ultrathin Nickel Nanowires, *Trans. Nonferrous Met. Soc. China*, 2013, **23**(11), p 3353–3361. https://doi.org/10.1016/s1003-6326(13)62875-7
18. H.F. Zhan, Y.T. Gu, C. Yan, X.Q. Feng, and P.K.D.V. Yarlagadda, Numerical Exploration of Plastic Deformation Mechanisms of Copper Nanowires with Surface Defects, *Comput. Mater. Sci.*, 2011, **50**(12), p 3425–3430
19. H. Zhan and Y. Gu, Atomistic Exploration of Deformation Properties of Copper Nanowires with Pre-Existing Defects, *Comput. Model. Eng. Sci.*, 2011, **80**(1), p 23–56
20. S.F. Ferdous and A. Adnan, Role of a Single Surface Vacancy on the Tensile Stress-Strain Relations of Single Crystal Ni Nanowire, *Comput. Mater. Sci.*, 2014, **90**, p 221–231. https://doi.org/10.1016/j.commatsci.2014.04.022
21. M. Makino, T. Tsuji, and N. Noda, MD Simulation of Atom-Order Void Formation in Ni Fcc Metal, *Comput. Mech.*, 2000, **26**(3), p 281–287. https://doi.org/10.1007/s004660000155
22. M.J. Buehler and H. Gao, Ultra-Large Scale Simulations of Dynamic Materials Failure, *Handb. Theor. Comput. Nanotechnol.*, 2005, **10**, p 1–41
23. M.I. Mendelev, M.J. Kramer, S.G. Hao, K.M. Ho, and C.Z. Wang, Development of Interatomic Potentials Appropriate for Simulation of Liquid and Glass Properties of nizr2 Alloy, *Philos. Mag.*, 2012, **92**(35), p 4454–4469
24. J.J. Bean and K.P. McKenna, Origin of Differences in the Excess Volume of Copper and Nickel Grain Boundaries, *Acta Mater.*, 2016, **110**, p 246–257
25. S.M. Rassoulinejad-Mousavi, Y. Mao, and Y. Zhang, Evaluation of Copper, Aluminum, and Nickel Interatomic Potentials on Predicting the Elastic Properties, *J. Appl. Phys.*, 2016, **119**(24)
26. R. Rezaei, C. Deng, H. Tavakoli-Anbaran, and M. Shariati, Deformation Twinning-Mediated Pseudoelasticity in Metal–graphene Nanolayered Membrane, *Philos. Mag. Lett.*, 2016, **96**(8), p 322–329. https://doi.org/10.1080/09500839.2016.1216195
27. W.J. Zhang, Z.L. Liu, and Y.F. Peng, Molecular Dynamics Simulations of the Melting Curves and Nucleation of Nickel Under Pressure, *Phys. B Condens. Matter*, 2014, **449**, p 144–149. https://doi.org/10.1016/j.physb.2014.05.025
28. S. Plimpton, LAMMPS: Molecular Dynamics Simulator. http://lammps.sandia.gov/, 2011
29. H. Liu and J. Zhou, Plasticity in Nanotwinned Polycrystalline Ni Nanowires Under Uniaxial Compression, *Mater. Lett.*, 2016, **163**, p 179–182. https://doi.org/10.1016/j.matlet.2015.10.068

30. R. Cao and C. Deng, The Ultra-Small Strongest Grain Size in Nanocrystalline Ni Nanowires, *Scr. Mater.*, 2015, **94**, p 9–12. https://doi.org/10.1016/j.scriptamat.2014.09.002
31. F. Sansoz and V. Dupont, Nanoindentation and Plasticity in Nanocrystalline Ni Nanowires: A Case Study in Size Effect Mitigation, *Scr. Mater.*, 2010, **63**(11), p 1136–1139. https://doi.org/10.1016/j.scriptamat.2010.08.028
32. Y. Liu and J. Zhao, The Size Dependence of the Mechanical Properties and Breaking Behavior of Metallic Nanowires: A Statistical Description, *Comput. Mater. Sci.*, 2011, **50**(4), p 1418–1424. https://doi.org/10.1016/j.commatsci.2010.11.026
33. W.G. Hoover, Canonical Dynamics: Equilibrium Phase-Space Distributions, *Phys. Rev. A*, 1985, **31**(3), p 1695
34. A.R. Setoodeh and H. Attariani, Nanoscale Simulations of Bauschinger Effects on a Nickel Nanowire, *Mater. Lett.*, 2008, **62**(27), p 4266–4268
35. W. Zhu, H. Wang, and W. Yang, Orientation- and Microstructure-Dependent Deformation in Metal Nanowires under Bending, *Acta Mater.*, 2012, **60**(20), p 7112–7122. https://doi.org/10.1016/j.actamat.2012.09.018
36. J. Diao, K. Gall, M.L. Dunn, and J.A. Zimmerman, Atomistic Simulations of the Yielding of Gold Nanowires, *Acta Mater.*, 2006, **54**(3), p 643–653
37. C.L. Kelchner, S.J. Plimpton, and J.C. Hamilton, Dislocation Nucleation and Defect Structure During Surface Indentation, *Phys. Rev. B Condens. Matter Mater. Phys*, 1998, **58**(17), p 11085–11088. https://doi.org/10.1103/physrevb.58.11085
38. A. Stukowski, Visualization and Analysis of Atomistic Simulation Data with OVITO-the Open Visualization Tool, *Model. Simul. Mater. Sci. Eng.*, 2010, **18**(1), p 15012. https://doi.org/10.1088/0965-0393/18/1/015012
39. A. Stukowski, V.V. Bulatov, and A. Arsenlis, Automated Identification and Indexing of Dislocations in Crystal Interfaces, *Model. Simul. Mater. Sci. Eng.*, 2012, **20**(8), p 85007
40. R.W. Hertzberg, *Deformation and Fracture Mechanics of Engineering Materials*, Wiley, New York, 1983, p 697
41. E.A. Alfyorova and D.V. Lychagin, Self-Organization of Plastic Deformation and Deformation Relief in FCC Single Crystals, *Mech. Mater.*, 2017, **2018**(117), p 202–213
42. D.V. Lychagin, E.A. Alfyorova, and A.S. Tailashev, Misorientation Development During the Formation of Macrobands in the [001] Nickel Single Crystals, *Russ. Phys. J.*, 2015, **58**(5), p 717–723
43. W.P. Wu and Z.Z. Yao, Molecular Dynamics Simulation of Stress Distribution and Microstructure Evolution Ahead of a Growing Crack in Single Crystal Nickel, *Theor. Appl. Fract. Mech.*, 2012, **62**(1), p 67–75. https://doi.org/10.1016/j.tafmec.2013.01.008
44. S. Brinckmann, R. Sivanesapillai, and A. Hartmaier, On the Formation of Vacancies by Edge Dislocation Dipole Annihilation in Fatigued Copper, *Int. J. Fatigue*, 2011, **33**(10), p 1369–1375. https://doi.org/10.1016/j.ijfatigue.2011.05.004
45. J.P. Hirth and J. Lothe, *Theory of Dislocations*, 2nd ed., Wiley, New York, 1982
46. G.E. Dieter and D.J. Bacon, *Mechanical Metallurgy*, McGraw-Hill, New York, 1986
47. L. Smith, J.A. Zimmerman, L.M. Hale, and D. Farkas, Molecular Dynamics Study of Deformation and Fracture in a Tantalum Nano-Crystalline Thin Film, *Model. Simul. Mater. Sci. Eng.*, 2014, **22**(4)
48. D. Huang, Q. Zhang, and Y. Guo, Molecular Dynamics Simulation for Axial Tension Process of α-Fe and Ni Nano Wires, *Ordnance Mater. Sci. Eng.*, 2006, **5**, p 4
49. M. Chen, E. Ma, K.J. Hemker, H. Sheng, Y. Wang, and X. Cheng, Deformation Twinning in Nanocrystalline Aluminum, *Science*, 2003, **300**, p 1275–1277. https://doi.org/10.1126/science.1083727
50. D. Chen, J. Wang, T. Chen, and L. Shao, Defect Annihilation at Grain Boundaries in Alpha-Fe, *Sci. Rep.*, 2013, **3**(13), p 1–5
51. P.H. Sung and T.C. Chen, Studies of Crack Growth and Propagation of Single-Crystal Nickel by Molecular Dynamics, *Comput. Mater. Sci.*, 2015, **102**, p 151–158. https://doi.org/10.1016/j.commatsci.2015.02.031
52. J. Zhang and S. Ghosh, Molecular Dynamics Based Study and Characterization of Deformation Mechanisms Near a Crack in a Crystalline Material, *J. Mech. Phys. Solids*, 2013, **61**(8), p 1670–1690. https://doi.org/10.1016/j.jmps.2013.04.004
53. A. Prakash, J. Guénolé, J. Wang, J. Müller, E. Spiecker, M.J. Mills, I. Povstugar, P. Choi, D. Raabe, and E. Bitzek, Atom Probe Informed Simulations of Dislocation-Precipitate Interactions Reveal the Importance of Local Interface Curvature, *Acta Mater.*, 2015, **92**, p 33–45
54. G. Sainath and B.K. Choudhary, Molecular Dynamics Simulation of Twin Boundary Effect on Deformation of Cu Nanopillars, *Phys. Lett. A*, 2015, **379**(34–35), p 1902–1905
55. S. Zhang and Y. Wang, Molecular Dynamics Simulation of Tension-Compression Asymmetry in Plasticity of Fivefold Twinned Ag Nanopillars, *Phys. Lett. Sect. A Gen. At. Solid State Phys.*, 2015, **379**(6), p 603–606
56. Y. Zhang, S. Jiang, X. Zhu, and Y. Zhao, Dislocation Mechanism of Void Growth at Twin Boundary of Nanotwinned Nickel Based on Molecular Dynamics Simulation, *Phys. Lett. Sect. A Gen. At. Solid State Phys.*, 2016, **380**(35), p 2757–2761. https://doi.org/10.1016/j.physleta.2016.06.044
57. Y. Zhang, S. Jiang, X. Zhu, and Y. Zhao, Influence of Void Density on Dislocation Mechanisms of Void Shrinkage in Nickel Single Crystal Based on Molecular Dynamics Simulation, *Phys. E Low-Dimens. Syst. Nanostruct.*, 2017, **90**(March), p 90–97. https://doi.org/10.1016/j.physe.2017.03.014
58. S. Aubry and D.A. Hughes, Reductions in Stacking Fault Widths in Fcc Crystals: Semiempirical Calculations, *Phys. Rev. B Condens. Matter Mater. Phys.*, 2006, **73**(22), p 1–15
59. V. Yamakov, D. Wolf, S.R. Phillpot, and H. Gleiter, Dislocation-Dislocation and Dislocation-Twin Reactions in Nanocrystalline Al by Molecular Dynamics Simulation, *Acta Mater.*, 2003, **51**(14), p 4135–4147. https://doi.org/10.1016/S1359-6454(03)00232-5
60. X. Zhao, C. Lu, A.K. Tieu, L. Pei, L. Zhang, L. Su, and L. Zhan, Deformation Mechanisms in Nanotwinned Copper by Molecular Dynamics Simulation, *Mater. Sci. Eng. A*, 2016, **2017**(687), p 343–351
61. X.Z. Liao, S.G. Srinivasan, Y.H. Zhao, M.I. Baskes, Y.T. Zhu, F. Zhou, E.J. Lavernia, and H.F. Xu, Formation Mechanism of Wide Stacking Faults in Nanocrystalline Al, *Appl. Phys. Lett.*, 2004, **84**(18), p 3564–3566
62. A. Hunter and I.J. Beyerlein, Stacking Fault Emission from Grain Boundaries: Material Dependencies and Grain Size Effects, *Mater. Sci. Eng. A*, 2014, **600**, p 200–210. https://doi.org/10.1016/j.msea.2014.02.030
63. C.B. Carter and S.M. Holmes, The Stacking Fault Energy of Nickel, *Philos. Mag.*, 1977, **35**(5), p 1161–1172
64. D. Hull and D.J. Bacon, Chapter 5 - Dislocations in Face-Centered Cubic Metals, *Introduction to Dislocations*, D. Hull and D.J. Bacon, Eds., Fifth Edit, (Oxford), Butterworth-Heinemann, 2011, p 85–107, https://doi.org/10.1016/B978-0-08-096672-4.00005-0
65. J.A. Zimmerman, H. Gao, and F.F. Abraham, Generalized Stacking Fault Energies for Embedded Atom FCC Metals, *Model. Simul. Mater. Sci. Eng.*, 2000, **8**, p 103–115
66. Z.Q. Wang, I.J. Beyerlein, and R. LeSar, Dislocation Motion in High Strain-Rate Deformation, *Philos. Mag.*, 2007, **87**(16), p 2263–2279
67. Q. Kun, Y. Li-Ming, and H. Shi-Sheng, Mechanism of Strain Rate Effect Based on Dislocation Theory, *Chin. Phys. Lett.*, 2009, **26**(3), p 36103